



Quasi-Omnidirectional Ultrathin Silicon Solar Cells Realized by Industrially Compatible Processes

Yan Li, Sihua Zhong,* Yufeng Zhuang, Lifei Yang, Fanying Meng,* Wenjie Wang, Zhengping Li, and Wenzhong Shen*

Ultrathin crystalline silicon (c-Si) solar cells provide advantages in reducing the use of c-Si material and being flexible, but there are several challenges that need to be conquered, such as limited optical absorption, high sensitivity to surface recombination, and complicated fabrication issues. Here, all-solution-processed Si nanopyramids (SiNPs) are proposed as the surface texture for ultrathin c-Si solar cells to solve the light absorption issue, whose preparation process is simple, low-cost, and industrially compatible. Combining the SiNPs texture with good passivation technique, an efficiency of 15.1% with an open circuit voltage approaching 700 mV is realized on a 37 μm thick c-Si solar cell. Moreover, both experimental and simulation investigation reveal that the SiNP-textured ultrathin solar cells have quasi-omnidirectional light absorption characteristic, showing a potential to produce higher all-day output power compared with the Si micropyramids textured counterpart. To further reduce the cost of ultrathin c-Si solar cells, a direct copper metallization is also investigated in replacement of silver metallization, which can result in a comparable efficiency. The present work demonstrates the conventional industrial processes for achieving low-cost ultrathin c-Si solar cells.

1. Introduction

Although crystalline silicon (c-Si) solar module cost has been remarkably reduced during the past decade, the levelized cost of electricity (LCOE) of solar energy is still higher than that of fossil-fuel based energy. Ultrathin c-Si solar cells provide a feasible pathway toward shrinking the material cost by reducing the volume of silicon consumed in a photovoltaic (PV) cell,^[1] as well as allowing the use of low-quality material owing to the fact that shorter minority carrier diffusion length is required to achieve efficient carrier collection in ultrathin solar cells.^[2–5] Here, the thicknesses of ultrathin c-Si are less than 50 μm, at least 3 times thinner than that of the mainstream (160–180 μm) in present PV industry. To date, considerable interest has been attracted in ultrathin c-Si solar cells and some good results have been yielded.^[6–10] For example, Branham et al.^[5] have reported a 15.7% efficient

10 μm thick c-Si solar cell by using periodic nanostructures. Moslehi et al.^[11] have achieved a 21.2% efficient solar cell with 35 μm thick c-Si absorber based on epitaxial silicon and porous silicon lift-off technology, and a 18 μm thick solar cell with an efficiency of 16.8% was reported using the same approach on steel by Wang et al.^[9] An efficiency of 13.6% was realized on a 20 μm thick hybrid silicon/polymer solar cell by He et al.^[12] Although ultrathin c-Si solar cells show great promise for reducing the material cost, the existing fabrication processes are too complicated and not cost-effective to apply to the present production lines; in the meantime, the performance of ultrathin solar cells is still poor comparing with that of the commercial c-Si solar cells (thickness: 160–180 μm).

The principal deficiency of hindering the development of highly efficient ultrathin c-Si solar cells is the weak optical absorption in the near-infrared wavelengths due to the reduced Si absorber thickness, which consequently results in a reduced photocurrent.^[13] To address this issue, excellent light-trapping effect is required to increase the effective optical absorption length. Hence, a range of surface texturing structures such as inverted nanopyramids,^[5,14–16] nanocones,^[8,17,18] nanocylinders,^[19] nanodomes,^[20] and nanoholes^[21] have been proposed as both the antireflection and light-trapping technique to enhance the solar photon absorption in ultrathin c-Si. Aside from their

Y. Li, Dr. S. H. Zhong, Y. F. Zhuang, W. J. Wang, Dr. Z. P. Li,
Prof. W. Z. Shen

Institute of Solar Energy
Key Laboratory of Artificial Structures and Quantum Control
(Ministry of Education)
Department of Physics and Astronomy
Shanghai Jiao Tong University
Shanghai 200240, P. R. China
E-mail: zhongsh@sjtu.edu.cn; wzshen@sjtu.edu.cn

Dr. L. F. Yang
GCL System Integration Technology Co., Ltd.
Suzhou 215000, P. R. China

Dr. F. Y. Meng
Research Center for New Energy Technology
Shanghai Institute of Microsystem and Information Technology (SIMIT)
Chinese Academy of Sciences
Shanghai 200050, P. R. China
E-mail: fymeng@mail.sim.ac.cn

Prof. W. Z. Shen
Collaborative Innovation Center of Advanced Microstructures
Nanjing 210093, P. R. China

The ORCID identification number(s) for the author(s) of this article can be found under <https://doi.org/10.1002/aelm.201800858>.

DOI: 10.1002/aelm.201800858

small feature size suitable for ultrathin solar cell, nanostructures are also conducive to material removal reduction, thus keeping the absorber thickness as much as possible. Nevertheless, the nanostructures mentioned above either require the use of lithography, which is sophisticated and expensive for manufacture, or incur severe surface recombination, a problem even more prominent in ultrathin solar cells.^[22] In contrast, Si upright nanopyramids texture formed by metal-assisted alkaline etching (MAAE) method possesses the characteristics of facile operation and low cost, together with low surface area enhancement. The fabricated Si nanopyramids (SiNPs) can help to achieve near-Lambertian light absorption in ultrathin c-Si.^[23] Moreover, it has been demonstrated in our previous study that SiNP-textured solar cells (with standard thickness) have quasi-omnidirectional photoelectric conversion ability, which is beneficial for increasing the all-day output of solar cells.^[24]

Besides light management in ultrathin c-Si solar cells, another important issue is to control surface carrier recombination. Branham et al.^[5] have carried out a simulation to show that the open circuit voltage (V_{OC}) and power conversion efficiency of ultrathin solar cells are dramatically decreased with the increasing surface recombination, supposing that bulk lifetime is not the limiting factor. In fact, because ultrathin solar cells have relatively larger surface to volume ratio, the V_{OC} of ultrathin solar cells is more susceptible to surface carrier recombination than that of commercial c-Si solar cells (thickness: 160–180 μm).^[1] Herein, we have adopted the commercially mature silicon heterojunction (SHJ) technology that features good surface passivation quality (although it is mature, it is rarely reported in ultrathin c-Si solar cells).^[25,26] In combination with SiNPs texture formed by an all-solution-processed method, MAAE, which is simple, cost-effective, and fully compatible with the existing production lines, we have successfully fabricated a 37 μm thick c-Si solar cell with an efficiency of 15.1% and a V_{OC} of nearly 700 mV. By analyzing external quantum efficiency (EQE) varying with the incident angle (θ) and optical simulations by finite-difference time-domain (FDTD), both

excellent and quasi-omnidirectional light absorption properties have been demonstrated in SiNP-textured ultrathin c-Si solar cell. To further reduce the cost, we have also explored copper metallization substituting for silver metallization through multiwire technology^[27] in ultrathin c-Si solar cells.

2. Results and Discussion

2.1. Surface Morphology

Figure 1 shows the 45° tilted-view and the cross-sectional scanning electron microscopy (SEM) images of the SiNP-textured and Si micropyramid (SiMP)-textured ultrathin c-Si surfaces. Note that the SiMPs texture is formed by a conventional alkaline etching method under the temperature of 83 °C,^[28,29] while for the SiNPs texture, it just additionally requires coating c-Si surface with Ag nanoparticles in a mixed solution of AgNO_3 and HF, and then follows the conventional alkaline etching method under lower temperature (65 °C), namely the MAAE method. More details of the fabrication are presented in the Experimental Section. As shown in Figure 1a,b,a',b', both SiNPs and SiMPs are densely distributed on the surfaces, but the sizes of SiNPs ($0.7 \pm 0.5 \mu\text{m}$) are much smaller than that of SiMPs ($5.5 \pm 4.0 \mu\text{m}$), which helps maintain the flatness of surface texture, and thus effectively reduces the mechanical stress of ultrathin solar cells. In addition, SiNPs texture exhibit much smoother surface. Consequently, it is expected to have smaller surface area and less dangling bonds, and it is easier to obtain lower surface recombination by passivation technique compared with the SiMPs texture. The thicknesses of both wafers become different after the texturizations even though they are the same at the beginning, as presented in Figure 1c,c'. The thickness of SiNP-textured ultrathin wafer is $37 \pm 1 \mu\text{m}$, 5 μm thicker than that ($32 \pm 1 \mu\text{m}$) of SiMP-textured ultrathin wafer, which is in agreement with our previous result that SiNPs texture has less material removal reduction.^[23] As is well-known,

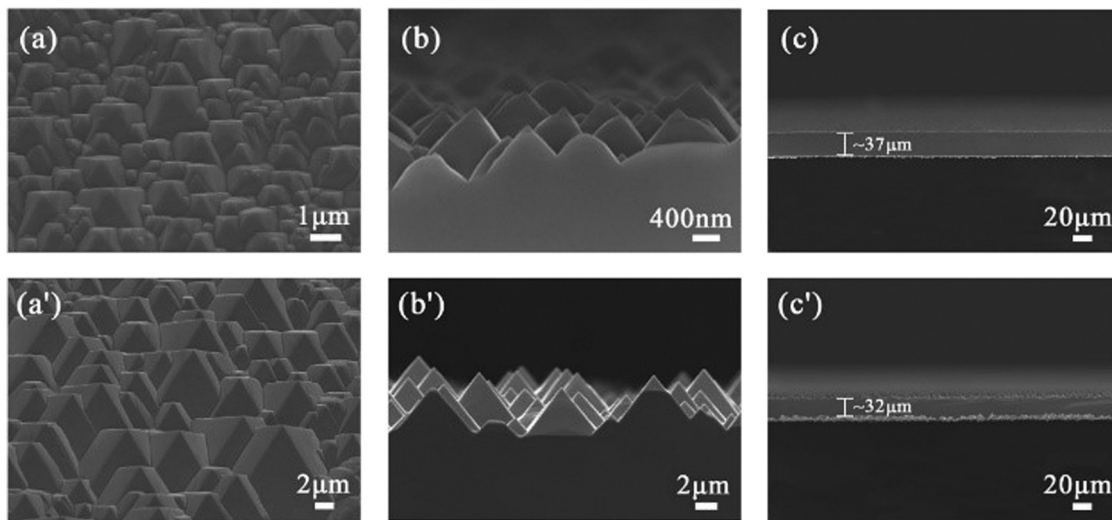


Figure 1. a) 45° tilted-view and b) cross-sectional SEM images of SiNP-textured surface. c) Cross-sectional SEM image of SiNP-textured ultrathin silicon. a') 45° tilted-view and b') cross-sectional SEM image of SiMP-textured surface. c') Cross-sectional SEM image of SiMP-textured ultrathin silicon.

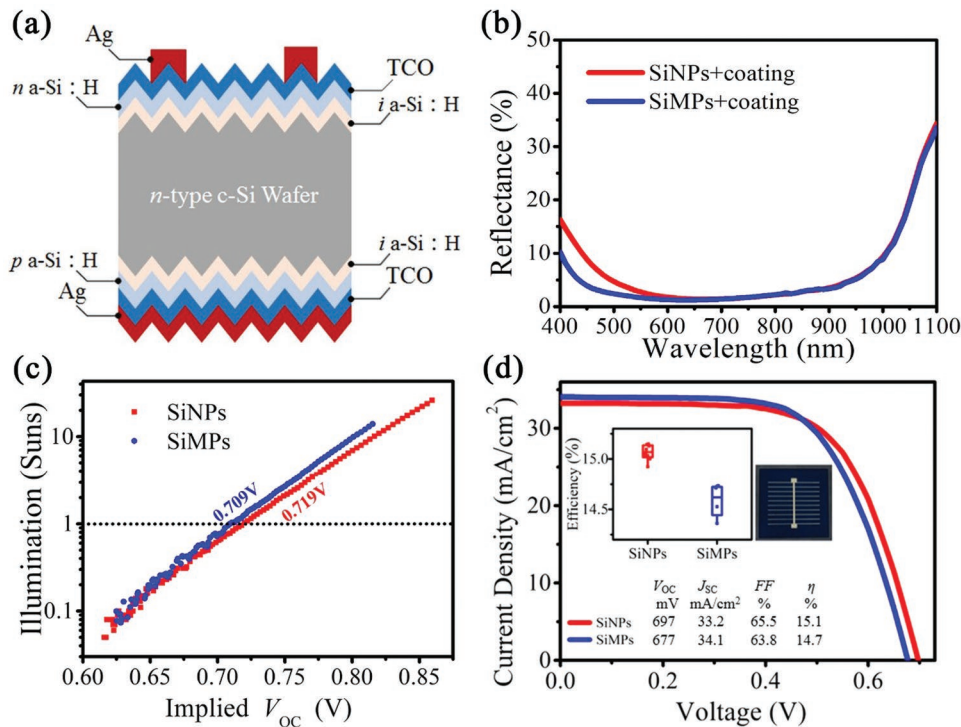


Figure 2. a) Structure diagram of ultrathin SHJ solar cells. b) Comparison of reflectance spectra of SiNP-textured and SiMP-textured ultrathin solar cells without the front-side Ag grids. c) Comparison of sun-implied V_{oc} plots of SiNP-textured and SiMP-textured ultrathin wafers with n/i a-Si:H on the front side and p/i a-Si:H on the back side. d) J–V curves of SiNP-textured and SiMP-textured ultrathin heterojunction solar cells. η is the conversion efficiency of solar cells. The inset exhibits the efficiency distribution and the best performance of SiNP-textured and SiMP-textured ultrathin solar cells, as well as the optical image of the fabricated solar cell on a 3 cm × 3 cm ultrathin c-Si wafer (the effective area of the solar cell is 2 cm × 2 cm).

reducing c-Si material loss in the texturization process is of great importance for ultrathin c-Si solar cells since this helps cells keep more absorbed light. Except for the advantages mentioned hereinbefore, it is worth mentioning that MAAE is a simple and cost-effective method for SiNPs texturization without involving any sophisticated patterning process, which is fully compatible with the existing production lines.

2.2. Solar Cell Performances

Figure 2a schematically illustrates the structure of ultrathin c-Si solar cells. It is based on the commercially mature SHJ design with rear emitter, which features good surface passivation quality. The n-type c-Si was used as the substrate, with intrinsic hydrogenated amorphous silicon (i a-Si:H) layers coating on both sides as passivation layers. The n-type a-Si:H layer (n a-Si:H) and p-type a-Si:H layer (p a-Si:H) serve as electron-selective and hole-selective layers, respectively. Tungsten-doped indium oxide (IWO) films deposited on both sides function as transparent conductive oxide (TCO) layers. Ag grids on the front side act as electrode, and Ag film totally covers the back side as both electrode and back reflection layer. Figure 2b compares the reflectance spectra of SiNP-textured and SiMP-textured ultrathin solar cells. Note that the reflectance spectra were measured without the front-side Ag grids but with back-side Ag film. As can be seen, both SiNP-textured and SiMP-textured ultrathin solar cells have a good antireflection effect

over a broadband wavelength range (450–1000 nm). The averaged reflectance of the SiNP-textured ultrathin solar cell in the measured wavelength range (400–1100 nm) is 7.0% under normal incidence condition, which is slightly higher than that of SiMP-textured ultrathin solar cell (6.0%). The slight difference (1.0%) is mainly due to the higher reflectance of SiNP-textured solar cell in the short wavelength region. This disadvantage could be compensated for to some extent by adjusting the deposition thicknesses of a-Si and TCO films, since the deposition conditions we adopted here were optimized for micropyramidal structure.

It is well known that the V_{oc} of c-Si solar cell increases as cell thickness decreases provided that the surface recombination is low.^[22] However, if the surface recombination is not sufficiently low (for example, >100 cm s⁻¹), the V_{oc} of ultrathin c-Si solar cells will be more prominently affected by the surface recombination velocity (S) compared with that of thick c-Si solar cells.^[1] Therefore, it is more critical to obtain good surface passivation quality for ultrathin solar cells. The surface recombination velocity can be calculated by the equation as follows, assuming that surface recombination properties at both c-Si surfaces are the same

$$\frac{1}{\tau_{eff}} = \frac{2}{W} S + \frac{1}{\tau_{bulk}} \quad (1)$$

where τ_{eff} is the effective lifetime, W is the wafer thickness, and τ_{bulk} is the bulk lifetime. In our ultrathin c-Si solar cells, at the

carrier density of 10^{15} cm^{-3} , the τ_{eff} s for the passivated SiNP-textured and SiMP-textured wafers are measured to be 918 and 522 μs , respectively, by using the photoconductance decay technique in transient mode. The Ws of SiNP-textured and SiMP-textured solar cells are 37 and 32 μm , respectively. The τ_{bulk} is assumed to be 10 ms.^[30] Hence the Ss at the carrier density of 10^{15} cm^{-3} for SiNP-textured and SiMP-textured solar cells are estimated to be as low as 1.83 and 2.18 cm s^{-1} , respectively, confirming the excellent passivation effect provided by both intrinsic a-Si and doped a-Si layers. The lower S of SiNP-textured solar cells is probably due to the smoother surface and/or less surface area, as indicated in Figure 1. Figure 2c further shows the sun-implied V_{OC} plots of ultrathin SHJ solar cells with two different surface textures. High implied V_{OC} (over 700 mV) can be obtained for both SiNP-textured and SiMP-textured ultrathin c-Si solar cells at 1 sun illumination. Besides, Figure 2c also denotes that the SiNP-textured ultrathin c-Si solar cell has higher implied V_{OC} than the SiMP-textured one, we attribute which to the smaller S.

Figure 2d illustrates current density–voltage (J – V) curves of SiNP-textured and SiMP-textured ultrathin c-Si solar cells. The inset shows the optical image of the fabricated ultrathin solar cell on an ultrathin c-Si wafer (3 cm \times 3 cm). The effective area of the solar cell is 2 cm \times 2 cm. It can be seen that the V_{OC} of SiNP-textured solar cell is 697 mV, exceeding that of SiMP-textured one (677 mV) by as much as 20 mV. Regarding fill factor (FF), the value of the SiNP-textured solar cell is 65.5%, 1.7% higher than that of the SiMP-textured solar cell (63.8%), which may be due to the lower surface recombination.^[30,31]

While for short-circuit current density (J_{SC}), owing to the higher reflectance under normal incidence condition, the J_{SC} of SiNP-textured solar cell is 33.2 mA cm^{-2} , 0.9 mA cm^{-2} lower than that of SiMP-textured solar cell (34.1 mA cm^{-2}). As an overall result, the ultrathin SHJ solar cell with SiNPs texture has an efficiency of 15.1%, an absolute value of 0.4% higher than that of SiMP-textured ultrathin c-Si counterpart (14.7%). We have also presented in the inset of Figure 2d the efficiency distribution of SiNP-textured and SiMP-textured ultrathin solar cells. For SiNP-textured ultrathin solar cells, the average efficiency is 15.07%, while for SiMP-textured ultrathin solar cells, the average efficiency is 14.62%. These results well illustrate the advantage of SiNPs texture over SiMPs texture in ultrathin c-Si solar cells. It should be pointed out that the J_{SC} and FF of the SiNP-textured ultrathin c-Si solar cell are still limited by an extrinsic loss. For example, the upper limit of J_{SC} of SiNP-textured ultrathin c-Si solar cell can reach 38 mA cm^{-2} by integrating the EQE in Figure 3.

2.3. Quasi-Omnidirectional Characteristic

As shown in Figure 3a, the EQE of SiNP-textured ultrathin solar cell in the middle and long wavelength (550–1100 nm) is well maintained as θ increases in the region of 0°–45°, exhibiting quasi-omnidirectional photoelectric conversion property. Subsequently, the EQE slightly declines when θ increases from 45° to 60°. Nevertheless, the SiMP-textured ultrathin solar cell exhibits a different behavior (see Figure 3b). In the whole

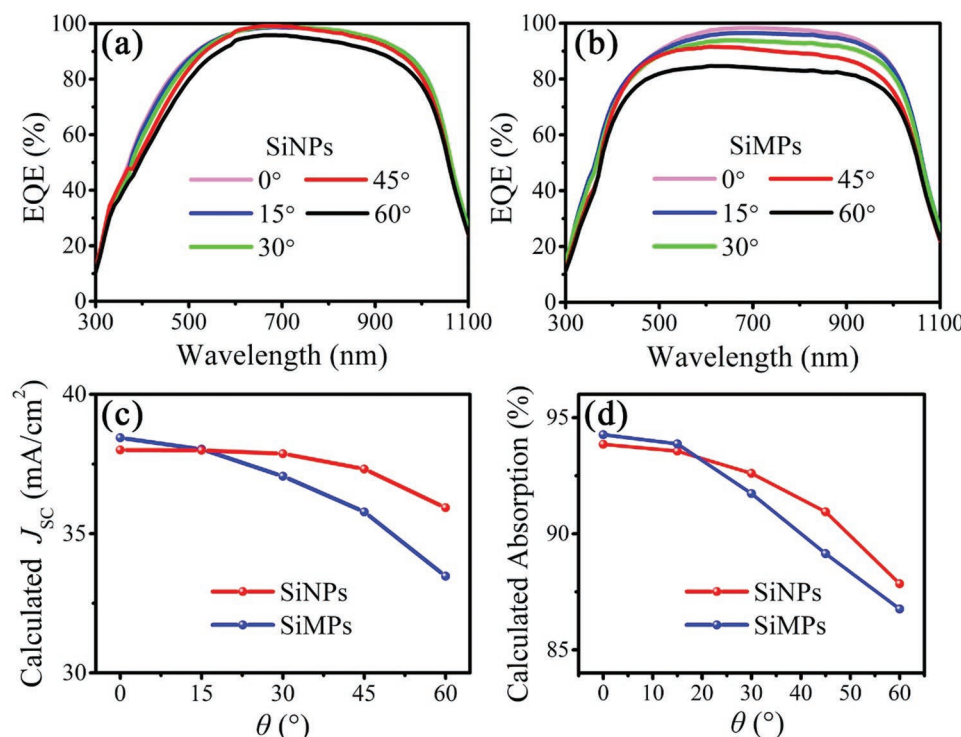


Figure 3. EQE spectra of a) SiNP-textured and b) SiMP-textured ultrathin solar cells varying with θ . c) Comparison of calculated J_{SC} of SiNP-textured and SiMP-textured ultrathin solar cells varying with θ . The calculated J_{SC} values were obtained by integrating EQE curves and the photon flux of the AM 1.5 spectrum. d) Calculated absorption of 37 μm thick SiNP-textured c-Si and 32 μm thick SiMP-textured c-Si (both with double-side SiN_x coating and Ag back reflector) varying with θ at the wavelength of 900 nm.

region of 0° – 60° , the EQE spectra of SiMP-textured ultrathin solar cell decrease obviously in the middle and long wavelength (500–1100 nm). To vividly illustrate the angular dependence of EQE of SiNP-textured and SiMP-textured ultrathin solar cells, we have also plotted the calculated J_{SC} of the two different cells as a function of θ , as shown in Figure 3c. Note that the calculated J_{SCs} were obtained by integrating EQE curves and the photon flux of the air-mass 1.5 (AM 1.5) spectrum over the wavelength of 300–1100 nm, with the assumption that the incident photon flux is the same for all θ s. It can be seen that in condition of vertical incidence ($\theta = 0^\circ$), the calculated J_{SC} of SiNP-textured ultrathin solar cell is lower than that of SiMP-textured ultrathin one, which is caused by the worse antireflection of the SiNPs under normal incidence condition. Despite that, as θ increases to 15° , the calculated J_{SCs} of SiNP-textured and SiMP-textured ultrathin solar cells are nearly the same. When θ becomes larger, the calculated J_{SCs} of the SiNP-textured ultrathin solar cell maintain higher than that of the SiMP-textured ones, owing to the less sensitivity of EQE of SiNP-textured ultrathin solar cell to θ . Considering the fact that the θ varies with time as the sun moves in the daytime, the SiNP-textured ultrathin solar cell is expected to produce higher all-day output power than SiMP-textured one, which helps to reduce LCOE.

The quasi-omnidirectional EQE characteristic of SiNP-textured ultrathin solar cell can be better understood through the light absorption varying with θ , obtained from optical simulations. Figure 3d illustrates the calculated absorption of 37 μm thick SiNP-textured and 32 μm thick SiMP-textured c-Si wafers (both with double-side SiN_x coating and Ag back reflector) at the wavelength of 900 nm. As can be seen, the optical absorption of the SiNP-textured c-Si is less sensitive to θ compared with that of the SiMP-textured one. As a result, although the

absorption of SiNP-textured c-Si is slightly lower than that of SiMP-textured c-Si when θ is between 0° and 15° , it becomes higher when θ is larger (30° – 60°). Therefore, the insensitivity of the EQE of SiNP-textured ultrathin solar cell to θ within 45° should be attributed to the quasi-omnidirectional light absorption ability.

2.4. Copper Metallization

Considering the cost savings of solar cell fabrication, we have also tried direct copper metallization, that is, replacing front Ag grids with polymer coated copper (C/Cu) wires through multi-wire technology.^[27] Figure 4a,b shows cross-sectional and top-view SEM images of C/Cu wires soldered on the front TCO layer of the SiNP-textured ultrathin solar cell by heat pressing at a temperature of 220 °C. The diameter of the C/Cu wire is about 150 μm , composing of a copper core with diameter of about 100 μm and a polymer outer shell with thickness of about 25 μm . The electric contact between the C/Cu wires and front TCO layer was realized via the outer conductive polymer coating layer of the C/Cu wires, which contains adhesive agent that can glue wire to TCO. Unlike screen printing method, multi-wire technology avoids high pressure during the metallization process, which matches well with the ultrathin solar cell fabrication process for reducing the risk of fragmentation. Figure 4c presents the optical image of the SiNP-textured ultrathin solar cell whose front side is directly copper metallized. The cell size is 3 cm × 3 cm, while the aperture area for the J - V measurement is designated as 2 cm × 2 cm in the center of solar cell by a mask. Two solder ribbons with width of 8 mm and thickness of 0.2 mm were placed at both sides of the copper metallized ultrathin solar cell for J - V measurement. There are 11 C/Cu

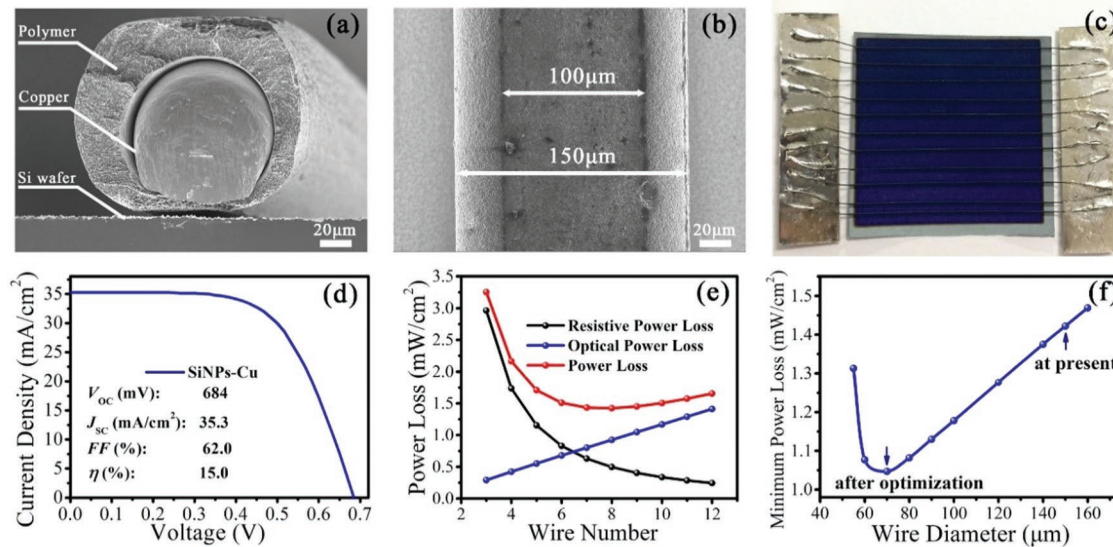


Figure 4. a) Cross-sectional and b) top-view SEM of a C/Cu wire soldered on the front TCO layer of the SiNP-textured ultrathin solar cell. c) Optical image of the SiNP-textured ultrathin solar cell whose front side is directly copper metallized. The cell size is 3 cm × 3 cm. d) J - V curve of SiNP-textured ultrathin solar cell with C/Cu wires. The aperture area for the J - V measurement is designated as 2 cm × 2 cm. η is the conversion efficiency of solar cells. e) Power loss of the copper metallized cell based on the given C/Cu wire diameter of 150 μm . f) Minimum power loss versus wire diameter plot of the copper metallized ultrathin solar cell.

wires soldered on the $3\text{ cm} \times 3\text{ cm}$ cell, and 8 C/Cu wires in the effective illumination area (4 cm^2). Hence the shading fraction of 8 C/Cu wires for the copper metallized ultrathin solar cell is 6.0%, lower than that of the silver metallized one (10.6%) by 4.6%, meaning less optical shading loss and thus higher J_{SC} . As shown in Figure 4d, the J_{SC} of copper metallized SiNP-textured ultrathin solar cell is 35.3 mA cm^{-2} , 2.1 mA cm^{-2} higher than that of the silver metallized SiNP-textured one (33.2 mA cm^{-2}).

It is worth noting that the FF of both the copper metallized and silver metallized ultrathin solar cell are lower at present compared to the conventional SHJ solar cells.^[27] It is probably caused by high series resistance (R_s) resulting from the non-optimized p a-Si:H/TCO and n a-Si:H/TCO contact resistances, which are two main components of R_s .^[32] As we know, the p a-Si:H/TCO and n a-Si:H/TCO contact resistances are sensitive to the deposition processes of the amorphous silicon and TCO layers. Note that the present deposition processes are fine-tuned based on the conventional thick c-Si substrate, they may not be suitable for the ultrathin c-Si substrate. For the copper metallized ultrathin solar cell, its FF is still relatively lower than its silver metallized counterpart. This is because there are 8 C/Cu wires in the effective illumination area (4 cm^2) for the former while there are 10 silver electrodes for the latter, which will cause larger resistive loss related to the sheet resistance of TCO layer in the former. It can be improved by optimizing the copper electrode layout.

Figure 4e,f indicates the further theoretical optimization of copper metallization for SiNP-textured ultrathin solar cell. As presented in Figure 4e, based on the given C/Cu wire diameter, we can calculate the power loss (P_{loss}) of the solar cell, where P_{loss} is the sum of resistive power loss ($P_{\text{resistance}}$) and optical power loss (P_{shading}) caused by copper metallization. By varying the amount of C/Cu wires, the P_{loss} is calculated by

$$P_{\text{resistance}} = R \cdot (J_{\text{mpp}})^2 \quad (2)$$

$$P_{\text{shading}} = A_{\text{shading}} \cdot J_{\text{mpp, no shading}} \cdot V_{\text{mpp}} \quad (3)$$

where R is the sum of R_{Cu} , R_{TCO} , and $R_{\text{TCO/Cu}}$, which are the series resistance components related to the resistance of C/Cu wires, the sheet resistance of TCO, and the contact resistance between C/Cu wires and TCO. R_{Cu} and $R_{\text{TCO/Cu}}$ can be calculated according to the literature.^[33] A_{shading} is the C/Cu wires shading fraction, J_{mpp} is the maximum power point current density, V_{mpp} is the maximum power point voltage of the simulated cell, and $J_{\text{mpp, no shading}}$ is the maximum power point current density of the simulated cell without C/Cu wires shading. The detailed calculation approach can be found in our previous study.^[27] By calculation, the optimized number for $2\text{ cm} \times 2\text{ cm}$ area of C/Cu wires (diameter: $150\text{ }\mu\text{m}$) is 8 corresponding to a minimum P_{loss} (see Figure 4e). As the diameter of C/Cu wires changes, the minimum P_{loss} changes accordingly. Consequently, the minimum P_{loss} of the copper metallized cell can be reduced from ≈ 1.42 to $\approx 1.05\text{ mW cm}^{-2}$ by decreasing the diameter of the C/Cu wires from 150 to $70\text{ }\mu\text{m}$ (see Figure 4f), corresponding to an E_{ff} increase of $\approx 0.37\%\text{abs}$. In this case, the efficiency of the copper metallized SiNP-textured ultrathin solar cell will exceed its silver metallized counterpart.

3. Conclusion

In conclusion, this study shows a facile, cost-effective, and industrially compatible way to simultaneously solve the optical absorption and surface recombination issues in ultrathin c-Si solar cells, and a $37\text{ }\mu\text{m}$ thick ultrathin c-Si solar cell with a V_{OC} of 697 mV and an efficiency of 15.1% is successfully realized in this way. The surface of cell is textured by SiNPs, which is proved to be suitable for application in ultrathin solar cell rather than conventional SiMPs texture for its smaller surface recombination and less absorber loss in texturization process. The MAAE method proposed for SiNPs texturization is an all-solution-processed method and fully compatible with the existing production lines. The high V_{OC} is achieved by employing the industrialized SHJ technique that features high passivation quality. By experimental and simulation investigation, it is found that the SiNP-textured ultrathin SHJ solar cells possess quasi-omnidirectional EQE performance, benefiting from the quasi-omnidirectional light absorption characteristic. Considering the fact that the sun moves constantly and thus θ varies with time, the SiNP-textured ultrathin solar cells show a great potential to produce higher all-day output power than the SiMP-textured ones. With an attempt to further reduce cost, we have also implemented a direct copper metallization in replacement of silver metallization on the front side of ultrathin solar cell. It is expected to surpass silver metallized ultrathin solar cell after optimization, showing great potential for achieving high efficient ultrathin solar cells with lower cost.

4. Experimental Section

Ultrathin c-Si Wafers Fabrication and Surface Texturization: The ultrathin c-Si wafers with thicknesses of about $40\text{ }\mu\text{m}$ were obtained from $165\text{ }\mu\text{m}$ thick n-type Czochralski (Cz) c-Si wafers with a resistivity of $1\text{--}7\text{ }\Omega\text{ cm}$, through being immersed in NaOH solution with a concentration of 10 wt% at $83\text{ }^\circ\text{C}$ for 60 min. After that, two different surface texturizations were carried out. For fabricating nanotexture, ultrathin c-Si wafers were first immersed in a mixed solution of AgNO_3 ($5 \times 10^{-3}\text{ M}$) and HF (4.7 vol%) for 5 s to deposit Ag nanoparticles on the surfaces. Then, the ultrathin c-Si wafers were etched to form SiNPs in an alkaline solution containing 1.1% NaOH and 6.3 vol% IPA at $65\text{ }^\circ\text{C}$ for 20 min. Ag nanoparticles were completely removed by rinsing the samples in dilute HNO_3 solution (volume ratio 1:1 with deionized water) for 10 min. Microtexture was prepared by etching the ultrathin Si wafers in an alkaline solution containing 1.1% NaOH and 6.3 vol% IPA at $83\text{ }^\circ\text{C}$ for 30 min.

Ultrathin c-Si Solar Cells Fabrication: The ultrathin c-Si wafers with two different surface textures mentioned above were cleaned by RCA cleaning procedure to remove residual metallic ions and SiO_2 . After that, i a-Si:H films ($\approx 5\text{ nm}$) were deposited by plasma-enhanced chemical vapor deposition (PECVD) on both sides of the wafer to enable high-quality interface passivation. Subsequently, n a-Si:H layer ($\approx 5\text{ nm}$) and p a-Si:H layer ($\approx 15\text{ nm}$) were deposited on the front side (i.e., illumination side) and back side as electron-selective and hole-selective layers, respectively. After that, IWO layers with thickness of 80 nm were deposited on both sides as TCO layers by reactive plasma deposition (RPD) process. Then Ag film with thickness of around 300 nm entirely covered the back side as positive electrode and optical reflection layer. Ag grids, as negative electrode, were deposited on the front side through a shadow mask, each finger of which had width of about $100\text{ }\mu\text{m}$ and height of about 600 nm . The spacing between fingers was about 1.8 mm . The positive and negative electrodes were both formed by electron beam evaporation. Finally, an air-annealing process was performed at the temperature of $200\text{ }^\circ\text{C}$ for 30 min.

In addition to Ag metallization, replacing front Ag grids with C/Cu wires through multiwire technology was also tried,^[27] the electrode on the back side was still Ag film. The C/Cu wires were soldered to the front TCO layer directly by heat pressing at 220 °C.

Characterization: The morphologies of front texture and cross-sectional ultrathin c-Si were investigated by field emission scanning electron microscopy. The reflectance, together with the EQE of the samples was measured via QEX10 (PV measurements). The minority carrier lifetime and implied V_{OC} under different illumination intensity were measured by WCT-120 (Sinton). The J-V performances of the solar cells were characterized by current-voltage tester under AM 1.5 illumination at 25 °C.

Simulations: Optical simulations were performed using the software FDTD to gain better insights into the difference of SiNP-textured and SiMP-textured ultrathin c-Si wafers. Substrate thicknesses of 37 and 32 μm were employed for SiNP-textured and SiMP-textured ultrathin c-Si wafers, respectively. For SiNP-textured wafer, 150 SiNPs were randomly distributed on a position of 5.7 μm × 4.0 μm region on x-y plane with pyramidal sizes of 0.2–1.5 μm. The ratio of height to bottom length of the Si pyramids was fixed to be 0.575, given that the angle between the slope facet and the bottom facet was 49°. For SiMP-textured wafer, 103 SiMPs were randomly distributed on a position of 34.2 μm × 24.0 μm region on x-y plane with pyramidal sizes of 0.8–10.0 μm. The ratio of height to bottom length of the Si pyramids was fixed to be 0.654, given that the angle between the slope facet and the bottom facet was 52.6°. In both cases, pyramids were partly overlapped as shown in the experimental results, and Bloch boundary in the x-y region was adopted for non-normal incident case. Besides, SiN_x with a constant refractive index of 2 and a thickness of 80 nm was placed at both sides. Meanwhile, an Ag layer with thickness of 1 μm was placed at the rear side. The optical parameters of c-Si were extracted directly from the FDTD simulation software. The light source was a plane wave with a fixed wavelength of 900 nm and its polarization angle was set to be 45° as the result of averaging P polarization and S polarization. The θ varied from 0° to 60°. A power monitor was positioned above the light source to obtain the reflectance (Ref) and an absorption monitor was used to obtain the light absorption in the Ag layer (A_{Ag}), so the absorption in ultrathin c-Si was calculated by 1–Ref– A_{Ag} .

Acknowledgements

This work was supported by the National Natural Science Foundation of China (11834011, 11674225, and 11474201).

Conflict of Interest

The authors declare no conflict of interest.

Keywords

copper metallization, industrial process, nanopyramid, quasi-omnidirectional, ultrathin silicon solar cell

Received: November 26, 2018

Revised: December 12, 2018

Published online:

sented at 39th IEEE Photovoltaic Specialists Conf., Tampa, FL, June 2013.

- [4] X. Tan, W. Yan, Y. Tu, C. Deng, *Opt. Express* **2017**, *25*, 14725.
- [5] M. S. Branham, W. C. Hsu, S. Yerci, J. Loomis, S. V. Boriskina, B. R. Hoard, S. E. Han, G. Chen, *Adv. Mater.* **2015**, *27*, 2182.
- [6] A. Wang, J. Zhao, S. R. Wrenham, M. A. Green, *Prog. Photovoltaics* **1996**, *4*, 55.
- [7] J. H. Petermann, D. Zielke, J. Schmidt, F. Haase, E. G. Rojas, R. Brendel, *Prog. Photovoltaics* **2012**, *20*, 1.
- [8] S. Jeong, M. D. McGehee, Y. Cui, *Nat. Commun.* **2013**, *4*, 2950.
- [9] L. Wang, A. Lohctefeld, J. Han, A. P. Gerger, M. Carroll, J. Ji, A. Lennon, H. Li, R. Opila, A. Barnett, *IEEE J. Photovoltaics* **2014**, *4*, 1397.
- [10] W. Yoon, A. Lohctefeld, N. Kotulak, D. Scheiman, A. Barnett, P. Jenkins, R. Walters, presented at 43rd IEEE Photovoltaic Specialists Conf., Portland, OR, June 2016.
- [11] M. M. Moslehi, P. Kapur, J. Kramer, V. Rana, S. Seutter, A. Deshpande, T. Stalcup, S. Kommera, J. Ashjaee, A. Calcaterra, D. Grupp, D. Dutton, R. Brown, presented at the PV Asia Pacific Conf., Singapore, October 2012.
- [12] J. He, P. Gao, M. Liao, X. Yang, Z. Ying, S. Zhou, J. Ye, Y. Cui, *ACS Nano* **2015**, *9*, 6522.
- [13] M. S. Branham, W.-C. Hsu, S. Yerci, J. Loomis, S. V. Boriskina, B. R. Hoard, S. E. Han, A. Ebong, G. Chen, *Adv. Opt. Mater.* **2016**, *4*, 858.
- [14] A. Gaucher, A. Cattoni, C. Dupuis, W. Chen, R. Cariou, M. Foldyna, L. Lalouat, E. Drouard, C. Seassal, I. C. P. Roca, S. Collin, *Nano Lett.* **2016**, *16*, 5358.
- [15] A. Mavrokefalos, S. E. Han, S. Yerci, M. S. Branham, G. Chen, *Nano Lett.* **2012**, *12*, 2792.
- [16] Q. Tang, H. Shen, H. Yao, K. Gao, Y. Jiang, Y. Liu, *J. Alloys Compd.* **2018**, *769*, 951.
- [17] K. X. Wang, Z. Yu, V. Liu, Y. Cui, S. Fan, *Nano Lett.* **2012**, *12*, 1616.
- [18] S. Wang, B. D. Weil, Y. Li, K. X. Wang, E. Garnett, S. Fan, Y. Cui, *Nano Lett.* **2013**, *13*, 4393.
- [19] K. J. Yu, L. Gao, J. S. Park, R. L. Yu, C. J. Corcoran, R. G. Nuzzo, D. Chanda, J. A. Rogers, *Adv. Energy Mater.* **2013**, *3*, 1528.
- [20] J. Zhu, C. M. Hsu, Z. Yu, S. Fan, Y. Cui, *Nano Lett.* **2010**, *10*, 1979.
- [21] K. Q. Peng, X. Wang, L. Li, X. L. Wu, S. T. Lee, *J. Am. Chem. Soc.* **2010**, *132*, 6872.
- [22] T. Mishima, M. Taguchi, H. Sakata, E. Maruyama, *Sol. Energy Mater. Sol. Cells* **2011**, *95*, 18.
- [23] S. Zhong, W. Wang, Y. Zhuang, Z. Huang, W. Shen, *Adv. Funct. Mater.* **2016**, *26*, 4768.
- [24] S. Zhong, W. Wang, M. Tan, Y. Zhuang, W. Shen, *Adv. Sci.* **2017**, *4*, 1700200.
- [25] F. Meng, J. Shi, L. Shen, L. Zhang, J. Liu, Y. Liu, J. Yu, J. Bao, Z. Liu, *Jpn. J. Appl. Phys.* **2016**, *56*, 04CS09.
- [26] F. Meng, L. Shen, J. Shi, L. Zhang, J. Liu, Y. Liu, Z. Liu, *Appl. Phys. Lett.* **2015**, *107*, 223901.
- [27] L. Yang, S. Zhong, W. Zhang, X. Li, Z. Li, Y. Zhuang, X. Wang, L. Zhao, X. Cao, X. Deng, Q. Wang, W. Shen, *Prog. Photovoltaics: Res. Appl.* **2018**, *26*, 385.
- [28] E. Vazsonyi, K. D. Clercq, R. Einhaus, E. V. Kerschaver, K. Said, J. Poortmans, J. Szlufcik, J. Nijs, *Sol. Energy Mater. Sol. Cells* **1999**, *57*, 179.
- [29] D. Chen, M. Edwards, S. Wrenham, M. Abbott, B. Hallam, *Front. Energy* **2017**, *11*, 23.
- [30] D. Adachi, J. L. Hernández, K. Yamamoto, *Appl. Phys. Lett.* **2015**, *107*, 233506.
- [31] A. Descoeuilles, Z. C. Holman, L. Barraud, S. Morel, S. D. Wolf, C. Ballif, *IEEE J. Photovoltaics* **2013**, *3*, 83.
- [32] D. Lachenal, D. Baetzner, W. Frammelsberger, B. Legradic, J. Meixenberger, P. Papet, B. Strahm, G. Wahli, *Energy Procedia* **2016**, *92*, 932.
- [33] A. Mette, *Ph.D. Thesis*, Universität Freiburg **2007**.